

Functional Graded Germanium–Lead Chalcogenide-Based Thermoelectric Module for Renewable Energy Applications

Eden Hazan,* Ohad Ben-Yehuda, Naor Madar, and Yaniv Gelbstein*

High thermoelectric conversion efficiencies can be achieved by making use of materials with, as high as possible, figure of merit, ZT , values. Moreover, even higher performance is possible with appropriate geometrical optimization including the use of functionally graded materials (FGM) technology. Here, an advanced *n*-type functionally graded thermoelectric material based on a phase-separated $(\text{PbSn}_{0.05}\text{Te})_{0.92}(\text{PbS})_{0.08}$ matrix is reported. For assessment of the thermoelectric potential of this material, combined with the previously reported *p*-type $\text{Ge}_{0.87}\text{Pb}_{0.13}\text{Te}$ showing a remarkable dimensionless figure of merit of 2.2, a finite-element thermoelectric model is developed. The results predict, for the investigated thermoelectric couple, a very impressive thermoelectric efficiency of 14%, which is more than 20% higher than previously reported values for operating under cold and hot junction temperatures of 50 °C and 500 °C, respectively. Validation of the model prediction is done by a thermoelectric couple fabricated according to the model's geometrical optimization conditions, showing a good agreement to the theoretically calculated results, hence approaching a higher technology readiness level.

1. Introduction

During recent years, many novel thermoelectric materials from various highly efficient thermoelectric material classes, useful for different temperature ranges, were developed for direct thermal to electrical energy conversion applications. In those material classes, enhancement of the dimensionless thermoelectric figure of merit, $ZT = \alpha^2 T / (\rho \kappa)$ (where α is Seebeck coefficient, ρ is electrical resistivity, κ is thermal conductivity, and T is absolute temperature), serving as a measure of the thermoelectric efficiency with respect to the involved materials' properties, was mainly achieved by either nanostructuring approaches for reduction of the phonon contribution to the thermal conductivity or advanced electronic doping methods for optimizing the electronic transport properties. Nevertheless, although very high ZTs were reported over the past few years, no practical thermoelectric generators with enhanced efficiencies have been reported to date. Therefore, for approaching suitable thermoelectric devices, besides advanced scientific

methods to enhance the materials' thermoelectric properties, practical design considerations including geometrical optimization and minimization of contact resistances and long-term properties degradation should be considered. For many years, thermoelectric power generation has enjoyed its greatest success in special and exotic applications, such as the space missions, in which the chalcogenides class of thermoelectric materials (e.g., GeTe ,^[1–4] PbTe ,^[5–10] PbS ,^[11–14] SnTe ,^[15–21] or their alloys) is the most thermoelectrically efficient in the intermediate temperature range of ≈ 500 °C, but still the system conversion efficiency for a state-of-practice NASA RTG (radioisotope thermoelectric generator) is about 6%,^[22] where in this type of application environmental issues and cost are not the main concerns. In this thermoelectric materials class, it was recently reported that upon proper

compositional investigation for systems exhibiting a miscibility gap between two individual chalcogenide components, sub-micron thermodynamic-driven phase separation features are expected, leading to dramatically reduced thermal conductivity values and enhanced ZTs . Two examples are the *p*-type $\text{Ge}_{0.87}\text{Pb}_{0.13}\text{Te}$,^[1] shown in Figure 1a, and the *n*-type 0.055% PbI_2 doped $(\text{PbSn}_{0.05}\text{Te})_{0.92}(\text{PbS})_{0.08}$ ^[11] compositions, exhibiting very high maximal ZTs of ≈ 2.2 and ≈ 1.5 , respectively, and correspondingly a very high thermoelectric potential.

For the latter, investigation of the PbS – PbTe quasi-binary phase diagram, Figure 1b reveals an extended miscibility gap at temperatures below 800 °C (1073 K in Figure 1b), in which a higher-temperature solution-treated single phase (the upper scanning electron microscopy, SEM image) is expected to follow a rapid phase separation to two individual PbTe - and PbS -rich phases (the lower SEM image) by either the spinodal decomposition or nucleation and growth mechanisms, upon cooling, depending on the specific composition. Due to the rapid nature of these phase separation reactions, the apparent alternating phases are usually finely dispersed, making them very useful phonon scattering centers for thermal conductivity reduction. Due to its thermodynamic origin, such a submicron phase generation is considered much more stable at elevated operating temperatures, compared to any other mechanical nano-features generation approaches such as ball-milling, which are expected to follow coarsening into the micron scale with long-term operations.

E. Hazan, O. Ben-Yehuda, N. Madar, Prof. Y. Gelbstein
Department of Materials Engineering
Ben-Gurion University of the Negev
Beer-Sheva, Israel
E-mail: edenhazan6@gmail.com; yaniv ge@bgu.ac.il



DOI: 10.1002/aenm.201500272

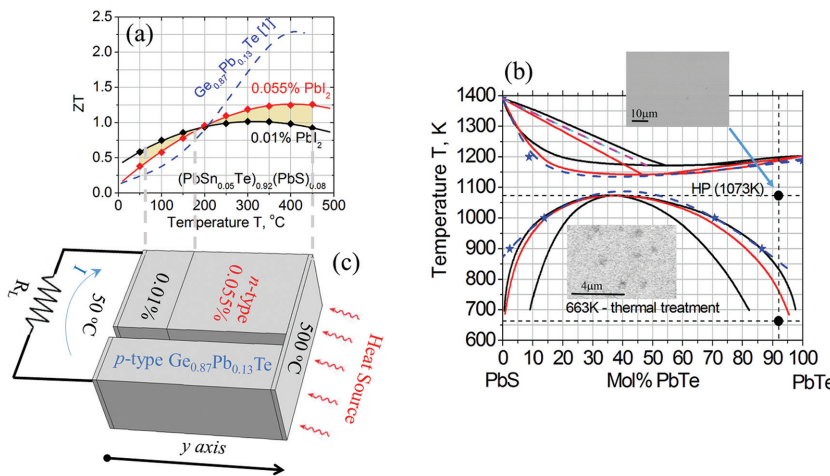


Figure 1. a) Temperature dependence of the dimensionless thermoelectric figure of merit, ZT , for the n-type 0.055% and 0.01% PbI_2 doped $(\text{PbSn}_{0.05}\text{Te})_{0.92}(\text{PbS})_{0.08}$ as obtained in this work and for the previously published p-type $\text{Ge}_{0.87}\text{Pb}_{0.13}\text{Te}$.^[1] b) Quasi-binary phase diagram of the $\text{PbTe}-\text{PbS}$ system as previously reported^[23] (black curve) and^[24] (red curve), as well as of the $\text{Pb}_{0.95}\text{Sn}_{0.05}\text{Te}-\text{PbS}$ system (blue curve), calculated for 100% $\text{Pb}_{0.95}\text{Sn}_{0.05}\text{Te}$ from the quasi-binary $\text{PbTe}-\text{SnTe}$ phase diagram^[25] and intermediate compositions reported previously at 900, 1000, and 1200 K.^[26] c) Configuration of the analyzed segmented thermoelectric couple in this work, based on two n-type 0.055% and 0.01% PbI_2 -doped $(\text{PbSn}_{0.05}\text{Te})_{0.92}(\text{PbS})_{0.08}$ segments and p-type $\text{Ge}_{0.87}\text{Pb}_{0.13}\text{Te}$.

For advancing the technological readiness level of chalcogenides-based thermoelectric power generation devices, the current research focused on a finite-elements design of a thermoelectric couple based on metallurgically and electronically optimized p-type $\text{Ge}_{0.87}\text{Pb}_{0.13}\text{Te}$ and n-type $(\text{PbSn}_{0.05}\text{Te})_{0.92}(\text{PbS})_{0.08}$ compositions, following a phase separation thermal treatment. Due to the fact that the originally reported latter composition was doped with 0.055% PbI_2 , leading to an optimal performance at higher temperatures (red curve in Figure 1a), an additional lower temperature optimal doping concentration of 0.01% PbI_2 was synthesized in the frame of the current research (black curve in Figure 1a). The thermoelectric efficiency is proportional to ZT and the Carnot efficiency (Equation (1)):

$$\eta = \frac{T_{\text{hot}} - T_{\text{cold}}}{T_{\text{hot}}} \frac{\sqrt{1+ZT} - 1}{\sqrt{1+ZT} + \frac{T_{\text{cold}}}{T_{\text{hot}}}} \quad (1)$$

From this, it is clear that in order to achieve high efficiency values, a wide operating temperature range (e.g., 50 °C–500 °C) for the thermoelectric materials is expected. For optimal efficiency design, a two-segmented n-type leg composed of a low temperature 0.01% doped segment and a high temperature 0.055% doped segment is considered, as shown in Figure 1c. The optimal length of each of the two segments is designed to correspond to the intersection temperature of the two ZT curves (shown in Figure 1a). Such a functionally graded materials (FGM) approach for optimizing the doping concentration for different temperature ranges was successfully applied for the less-efficient PbI_2 -doped pure PbTe compound,^[27,28] showing that due to the low diffusion coefficient of iodine in PbTe , stability of the graded profile is expected at temperatures of up to 500 °C.

Modeling of such a segmented thermoelectric couple should involve heat balance equations at both the hot/cold sides, the junction between the two n-type segments, and inside each element, taking into account contact electrical resistances, heat conduction, and Joule, Peltier, and Thomson heat contributions. Furthermore, a proper analysis should take into account the temperature dependence of each of the thermoelectric properties involved. So far, most of the thermoelectric modeling procedures were applied in low temperature (<300 °C) applications, in which non-FGM Bi_2Te_3 -based materials were involved, taking into account average thermoelectric properties^[29–33] of only single n- and p-type segments per couple. Only in such low temperature applications, due to the low temperature gradients and the relatively weak temperature dependence of the transport properties, this assumption is valid. Yet, for higher temperature applications, which are the main focus of the current research and consist of much stronger temperature dependence of the thermoelectric properties, a much more

sophisticated model taking into account all of these contributions should be developed. In the current research, a finite-element model based on COMSOL Multiphysics 4.2a software, taking into account temperature-dependent thermoelectric properties and the influence of the contact resistances, was developed for analyzing the expected electrical output parameters of the graded chalcogenides-based thermoelectric couple described in Figure 1c. The simulated prediction was validated by fabricating a geometrical optimized thermoelectric couple, which was characterized under a large temperature difference in a laboratory-built simulator.

2. Experimental Section

n-Type 0.01 and 0.055 mol% PbI_2 -doped $(\text{Pb}_{0.95}\text{Sn}_{0.05}\text{Te})_{0.92}(\text{PbS})_{0.08}$ samples were prepared by sealing the source materials (purity of 5N) at appropriate concentrations in a quartz ampoule under a vacuum of 10^{-6} Torr, and melting in a rocking furnace (Thermcraft incorporated, USA) at 1000 °C (1273K in Figure 1b) for 30 min followed by water quenching. Milling of the cast ingots into a maximal powder particle size of 250 μm was performed using an agate mortar and pestle. The sieved powder was subsequently hot pressed (HPW5 Hot Press FCT Systeme GmbH) under a mechanical pressure of 25 MPa at 800 °C (1073 K in Figure 1b) for 30 min, resulting in high density values >97% of the theoretical density. Subsequent thermal treatment was performed at 390 °C (663 K in Figure 1b) for 336 h, under argon atmosphere, to ensure phase separation in the vicinity of the miscibility gap of the quasi-binary $\text{Pb}_{0.95}\text{Sn}_{0.05}\text{Te}-\text{PbS}$ system (Figure 1b). The phase diagram was constructed based on previously reported thermodynamic data of the $\text{PbTe}-\text{PbS}$ ^[23,24] and $\text{PbTe}-\text{SnTe}$ systems.^[25,26]

Graded n-type legs based on a low temperature 0.01% and a high temperature 0.055% PbI₂-doped (Pb_{0.95}Sn_{0.05}Te)_{0.92}(PbS)_{0.08} segments (Figure 1c) were prepared by simultaneously hot pressing of the two individual powder compositions under the same conditions applied for each of the compositions separately.

p-Type legs based on the composition Ge_{0.87}Pb_{0.13}Te were prepared according to the procedure published previously.^[1]

Seebeck coefficient (α) and the electrical resistivity (ρ) were measured by a Linseis LSR-3/800 measuring system from room temperature up to 773 K. The thermal conductivity (κ) was determined as a function of temperature from room temperature to 773 K using the flash diffusivity method (LFA 457, Netzsch). The front face of a disc-shaped sample ($\varnothing = 12$ mm, thickness $\approx 1\text{--}2$ mm) was irradiated by a short laser burst, and the resulting rear face temperature was recorded and analyzed. Thermal conductivity values were calculated using the equation $\kappa = \gamma C_p \cdot \delta$, where γ is the thermal diffusivity, C_p is the specific heat (measured using differential scanning calorimetry, STA 449 – Netzsch), and δ is the bulk density of the sample (calculated from the sample's geometry and its mass).

Scanning of Seebeck coefficient along the graded samples, at room temperature, was performed by passing a minute heating probe along the samples in a procedure described elsewhere.^[28] The heating probe tip, attached to a micrometer with a resolution of 0.5 mm, was kept at 35 °C–40 °C, while the sample was maintained at room temperature. In this procedure, one side of the sample served as a reference point and each Seebeck coefficient data point was determined by measuring the voltage and the temperature at the probe's tip and the reference point.

The structural characteristics of the investigated samples were analyzed by high-resolution SEM (Jeol-7400F HRSEM) and X-ray diffraction (XRD; Rigaku DMAX 2100 powder diffractometer).

A numerical solution using finite-element modeling was based on COMSOL Multiphysics 4.2a software. The model was built in the built-in 3D heat transfer in solids physical mode.

The thermoelectric couple was assembled under an inert atmosphere using Ag conductive paste (Sigma-Aldrich) at 150 °C for 1 h.

Validation of the modeling predictions was performed in a laboratory-built simulator (shown schematically in Figure 2) under Ar protective atmosphere and a large temperature difference of 450 °C (the hot and cold sides were kept at 500 °C and 50 °C, respectively), measuring the output power.

3. Experimental Results

High-resolution SEM images following hot pressing at 800 °C, above the miscibility gap of the quasi-binary Pb_{0.95}Sn_{0.05}Te-PbS system (the upper image of Figure 1b), resulted in a single-phase solution treated PbTe-rich matrix, as can be also seen by the XRD diffraction pattern of Figure 3a (black diffraction pattern). Following a lower temperature thermal treatment at 390 °C, in the vicinity of the miscibility gap, phase separation of the high temperature Pb_{0.95}Sn_{0.05}Te solution-treated phase into a PbTe-rich matrix and PbS rich sub-micron domains was

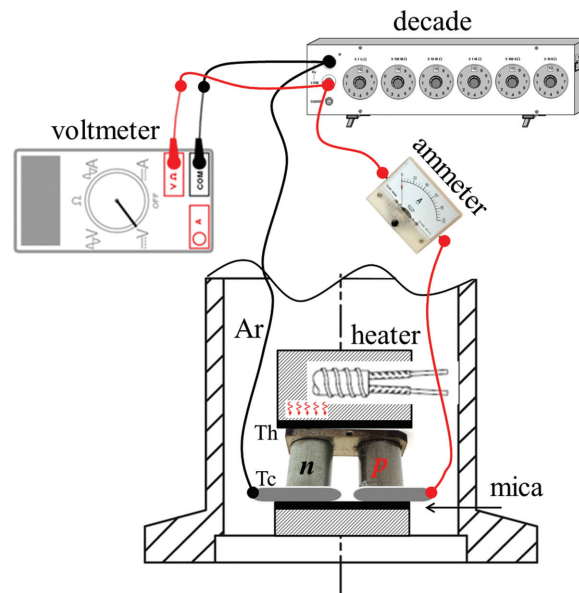


Figure 2. Experimental setup for characterization under large temperature gradients between the hot, Th, and cold, Tc, sides of the couple shown in Figure 1c, under protective argon atmosphere. Mica was used as an electrical insulator between the couple and Cu-based thermal reservoirs. The hot (upper) reservoir is heated by 250 W cartridge heater (Watlow, USA). For electrical measurement, the couple is serially connected to an ammeter and a load variable resistances decade, on which the load voltage was measured by a Keithley voltmeter.

apparent as can be seen by the lower image of Figure 1b, the SEM images of Figure 3a, and the red XRD diffraction pattern of Figure 3a.

The temperature-dependent transport properties, Seebeck coefficient, α , electrical resistivity, ρ , and thermal conductivity, κ , of the n-type 0.01 and 0.055 mol% PbI₂-doped (Pb_{0.95}Sn_{0.05}Te)_{0.92}(PbS)_{0.08} samples are shown in Figure 3b,c,d, respectively. From these figures, it can be clearly seen that reducing the PbI₂ doping concentration, and correspondingly the free electron concentration, resulted as expected with increased absolute Seebeck coefficient and electrical resistivity values and decreased thermal conductivity values. In addition, lower temperatures of the maximal/minimal transport properties were apparent for the lower doping concentration of 0.01% due to the earlier onset of the intrinsic conduction upon heating, as expected for samples with a lower carrier concentration. This lower carrier concentration for the 0.01% PbI₂-doped sample resulted in higher ZT values in the lower temperature range, compared to the 0.055% PbI₂-doped sample up to ≈ 200 °C, as can be seen in Figure 1a, in agreement with the trend reported previously for PbI₂-doped pure PbTe compounds.^[27] This finding highlights the potential of a two-segment functional graded material, following the maximal envelope of the ZT curves of the two doping concentrations, to achieve higher average ZTs over a wide temperature range, as can be seen by the yellow areas of Figure 1a, indicating the increased ZTs of the graded material compared to each of the individual compositions separately. Furthermore, the strong temperature dependence of the measured transport properties for both

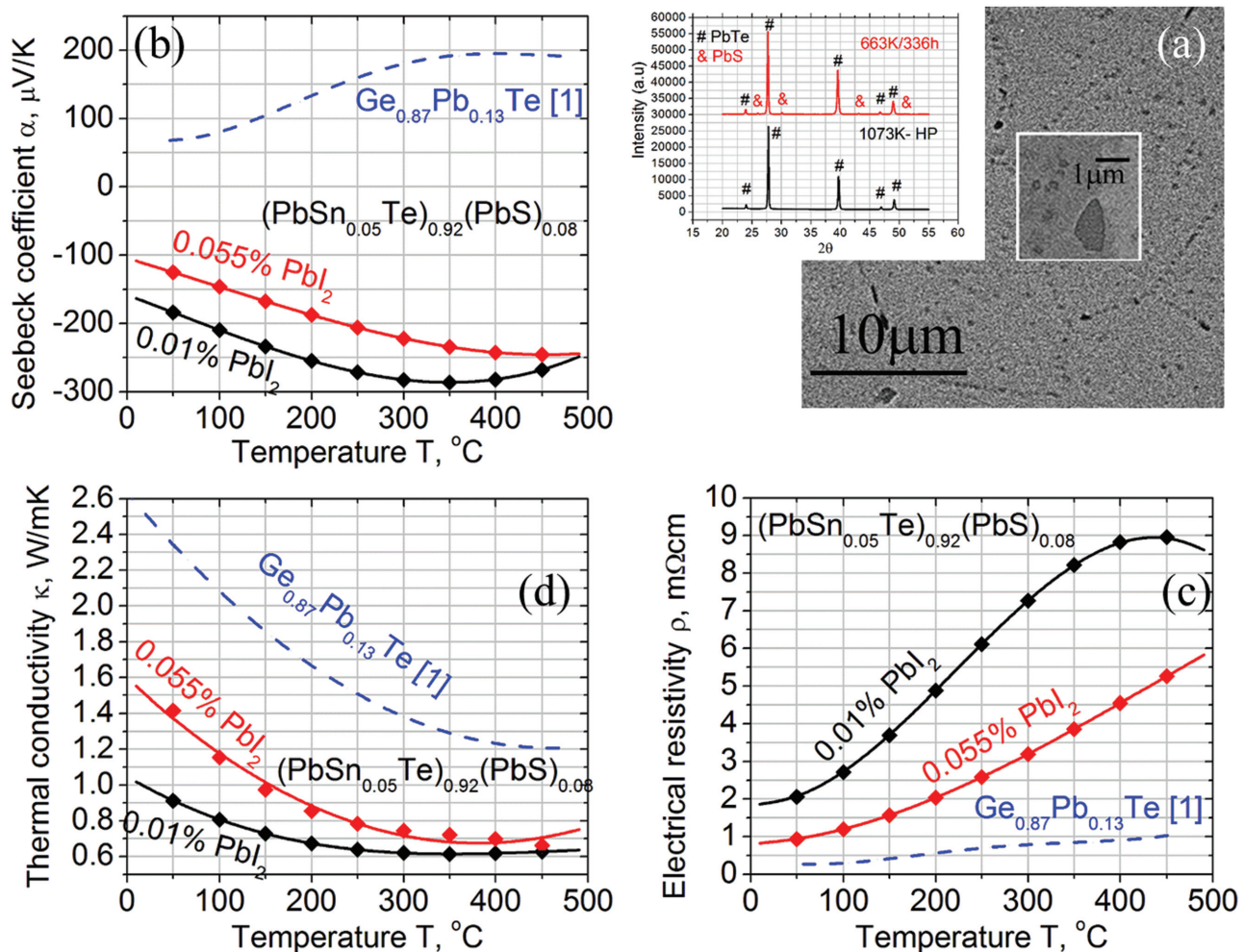


Figure 3. a) High-resolution SEM images of the prepared n-type $(\text{Pb}_{0.95}\text{Sn}_{0.05}\text{Te})_{0.92}(\text{PbS})_{0.08}$ samples following phase separation treatment at 390 °C. The XRD spectra following hot pressing at 800 °C and following phase separation treatment at 390 °C are also shown. The temperature-dependent Seebeck coefficient, α , electrical resistivity, ρ , and thermal conductivity, κ , of the investigated n-type 0.01% and 0.055% PbI_2 -doped $(\text{Pb}_{0.95}\text{Sn}_{0.05}\text{Te})_{0.92}(\text{PbS})_{0.08}$ samples compared to the previously reported p-type $\text{Ge}_{0.87}\text{Pb}_{0.13}\text{Te}$ composition^[1] are indicated in (b,c,d), respectively.

the investigated n-type and the single p-type $\text{Ge}_{0.87}\text{Pb}_{0.13}\text{Te}$ compositions, over the investigated temperature range (Figure 3), implies the importance of using an accurate model for thermoelectric devices based on these compositions.

4. Finite Element Modeling

Finite-element modeling (FEM) of the expected electrical performance of the investigated thermoelectric couple, shown in Figure 1c, was based on the temperature-dependent transport properties, shown in Figure 3b,c,d, typical hot and cold side temperatures of mid-temperature application, and optimal geometrical parameters of the thermoelectric segments connected by copper strips.

The geometrical parameters, including the optimal upper n-type segment height and the optimal ratio for p-type to n-type cross-section areas,^[34] being used as input parameters to the model, are listed in Table 1.

The heat transfer equation applied for calculation of the temperature distribution profiles along each of the n-type segments and the p-type leg is shown in Equation (2):

Table 1. Finite elements model parameters.

Parameter	Description	Value
T_{hot}	Hot side temperature	500 °C
T_{cold}	Cold side temperature	50 °C
L	Total height of the thermoelectric n and p legs	12 mm
B	Depth of the thermoelectric legs	5 mm
a_n	Width of the n-type leg	3.37 mm
a_p	Width of the p-type leg	1 mm
h_{copper}	Height of the copper contact strips	0.3 mm
L_{copper}	Width of the copper contact strips	5.37 mm
L_{n_up}	Height of the upper n-type segment	8.12 mm

$$\frac{d}{dy} \left(\kappa_{p,n} \cdot A_{p,n} \cdot \frac{dT_{p,n}}{dy} \right) = I \cdot T_{p,n} \cdot \frac{d\alpha_{p,n}}{dT_{p,n}} \cdot \frac{dT_{p,n}}{dy} \pm I^2 \cdot \frac{\rho_{p,n}}{A_{p,n}} \quad (2)$$

where A is the leg's cross-section area, y is the axis along the temperature gradient, and I is the electrical current, shown in Figure 1c.

Solving this nonlinear, second-order differential equation (Equation (2)), required for development of an accurate thermoelectric model, involves the powerful and reliable COMSOL Multiphysics computational tool.

The boundary conditions that apply for the simulated thermoelectric couple are listed in Equations (3) and (4).

$$T_p(0) = T_n(0) = T_{\text{cold}} \quad (3)$$

$$T_p(L) = T_n(L) = T_{\text{hot}} \quad (4)$$

While modeling a functionally graded thermoelectric leg, it is essential to include Joule and Peltier heat generated by the creation of a new joint between the upper and lower n-type segments. For approaching this condition, the current model involves an infinitesimal middle domain with the height of $\Delta y \rightarrow 0$, between the upper and lower n-type segments, defined as a heat source, as shown in Equation (5).

$$q_{\text{FGM}} = \frac{I \cdot T \cdot (\alpha_{n_down} - \alpha_{n_up})}{A_n \cdot \Delta y} + \frac{I^2 \cdot \rho_{\text{contact}}}{A_n \cdot \Delta y} \\ = -\frac{1}{\Delta y} \left(\kappa \cdot \frac{dT}{dy}_{n_down} - \kappa \cdot \frac{dT}{dy}_{n_up} \right) \quad (5)$$

where α_{n_down} , α_{n_up} , and ρ_{contact} are the Seebeck coefficient values of the upper and lower n-type segments at the intermediate joint and the electrical contact resistance, respectively.

The heat balance equations at the couple's hot and cold junctions are given in Equations (6) and (7), respectively.

$$q_{\text{hot}} = I \times [(\alpha_p - \alpha_n) \times T]_{T_{\text{hot}}} - \left(\kappa_p \times A_p \times \frac{dT}{dy} \right)_{y=L} \\ - \left(\kappa_n \times A_n \times \frac{dT}{dy} \right)_{y=L} - I^2 \times (R_{Hj} + R_{\text{contact}}) \quad (6)$$

$$q_{\text{cold}} = I \times [(\alpha_p - \alpha_n) \times T]_{T_{\text{cold}}} - \left(\kappa_p \times A_p \times \frac{dT}{dy} \right)_{y=0} \\ - \left(\kappa_n \times A_n \times \frac{dT}{dy} \right)_{y=0} + I^2 \times (R_{Cj} + R_{\text{contact}}) \quad (7)$$

where q_{hot} and q_{cold} are the absorbed and emitted heat fluxes at the couple's hot and cold sides, respectively, and R_{Hj} , R_{Cj} , $R_{\text{contact}} = \rho_{\text{contact}} / A$ are the electrical resistances of the upper and lower copper strips and contacts, respectively.

Under these conditions, the total output power, P , developed at the load resistance R_L (see Figure 1c) can be given according to either Equation (8) or Equation (9).

$$P = q_{\text{hot}} - q_{\text{cold}} \quad (8)$$

$$P = I \times E_{\text{open}} - I^2 \times R_{\text{in}} \quad (9)$$

where the open-circuit voltage, E_{open} , and the internal electrical resistance, R_{in} , of the thermoelectric couple are defined in Equations (10) and (11).

$$E_{\text{open}} = \int_{y=0}^{y=L} \left(\alpha_p \frac{dT}{dy} \right) dy - \int_{y=0}^{y=L} \left(\alpha_n \frac{dT}{dy} \right) dy \quad (10)$$

$$R_{\text{in}} = \int_{y=0}^{y=L} \frac{\rho_p(T(y))}{A_p} dy + \int_{y=0}^{y=L} \frac{\rho_n(T(y))}{A_n} dy \\ + 2 \cdot \frac{\rho_{\text{copper}} L_{\text{copper}}}{A_{\text{copper}}} + 2 \cdot \frac{\rho_{\text{contact}}}{A_p} + 3 \cdot \frac{\rho_{\text{contact}}}{A_n} \quad (11)$$

The above equations take into account the internal electrical resistance of the copper contact strips (with, ρ_{copper} is the electrical resistivity of pure copper) at the hot and cold junctions. Verification of the model's accuracy, % Error, was approached by comparing the calculated electrical power values obtained by both the thermal analysis, P_{thermal} , using Equation (8), and the electrical analysis, $P_{\text{electrical}}$, using Equation (9), according to Equation (12).

$$\% \text{Error} = 100 \cdot \frac{P_{\text{thermal}} - P_{\text{electrical}}}{P_{\text{thermal}}} \quad (12)$$

For all of the calculations, the error percentage, Equation (12), was found to be less than 0.1%, indicating the high reliability and accuracy of the calculated couple's parameters. Moreover, in order to avoid prolonged computation times, the model was solved taking into account adiabatic boundary conditions, even though different heat rejection conditions (e.g., convective cooling) are possible.

Simulated output electrical power and thermoelectric efficiency of the investigated thermoelectric couple, taking into account both together and separately the temperature dependence materials properties and contacts contributions, compared to a basic mean values model that is the mostly common in the literature, are shown in Figure 4, in addition to the thermal distribution values for the couple at the optimal efficiency conditions.

It can be clearly seen from Figure 4 that for the investigated couple, applying average materials' properties, results in about 3% lower thermoelectric efficiency values, around and at higher electrical currents than the optimal value ($I \approx 1.6$ A) and higher values with increased differences for higher electrical currents. These results, in addition to the fact that higher error percentage values, Equation (12), were obtained by applying average material properties, clearly indicate that taking into account the temperature dependency is favorable for obtaining

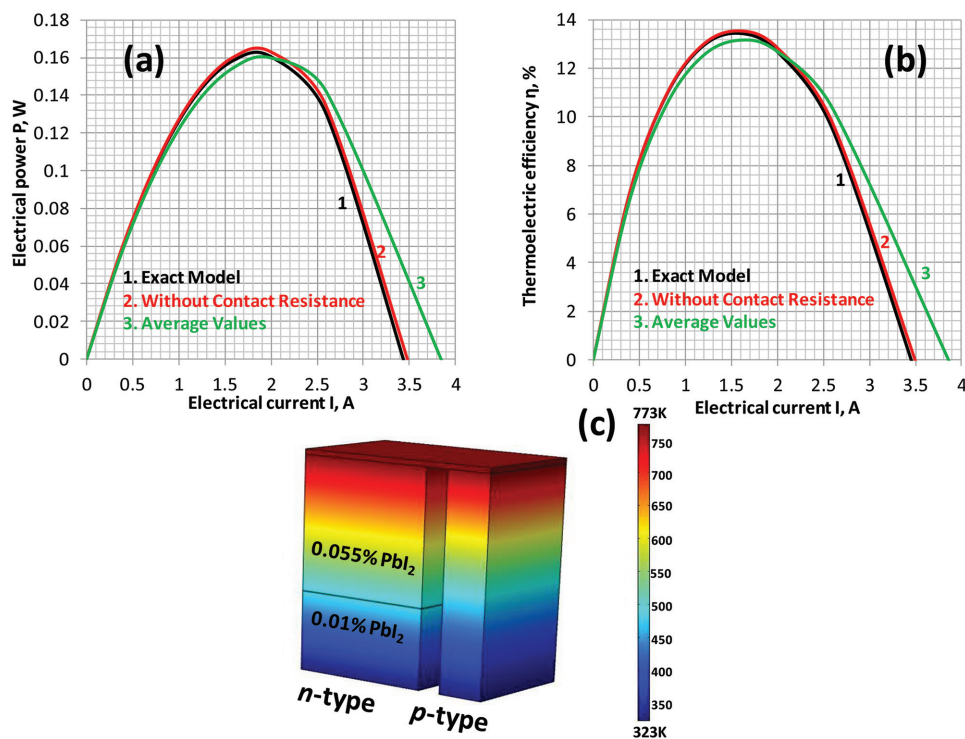


Figure 4. a) Electrical power and b) thermoelectric efficiency variations with the electrical current, taking into account together and separately the material properties, temperature dependence and contacts contributions, compared to the basic model eliminating these two contributions. c) Simulated thermal distribution along the investigated thermoelectric couple.

accurate simulated results and self-adaptive physical model. On the other hand, the contribution of the contact resistance, using the literature value of $10^{-3} \Omega \text{ mm}^2$ reported previously for high-quality contacts,^[35] to the model's accuracy was found as less influential with less than 1% variation at the maximal efficiency conditions. Nevertheless, including the contact resistance effect on the resultant electrical power is significant for a practical verification of the quality of the joining process while soldering/brazing of the metallic contacts to the thermoelectric legs. In the case of poor joining procedures, significantly

higher contact resistances compared to the literature value of $10^{-3} \Omega \text{ mm}^2$ ^[35] are expected, with a much stronger effect on reduction of the electrical power and efficiency values.

Based on a simulation taking into account both the temperature-dependent material properties and contact resistance contributions, maintaining a constant cold side temperature at 50 °C and varied hot side temperatures of 400 °C, 450 °C, and 500 °C, for optimal geometrical conditions, resulted in the couple's electrical power and efficiency values as indicated in Figure 5.

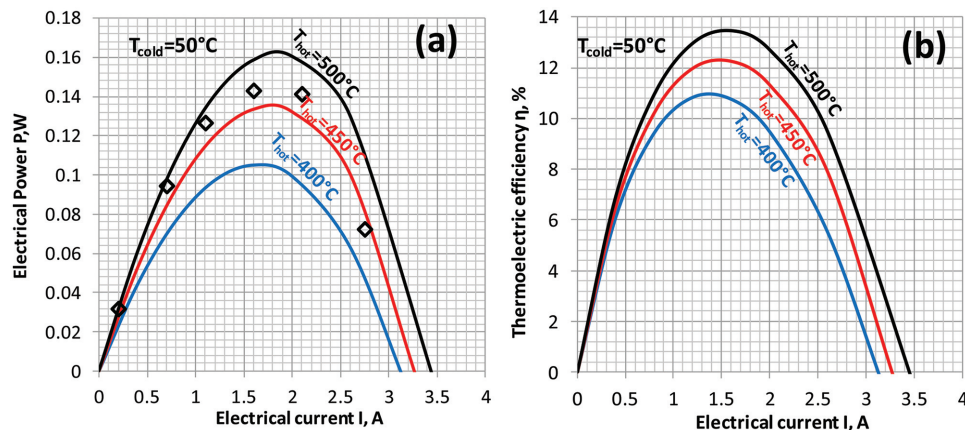


Figure 5. COMSOL simulated electrical power and efficiency values for the investigated couple under a constant cold side temperature of 50 °C and three hot side temperatures of 400 °C, 450 °C, and 500 °C. The empty black symbols indicate experimental points measured in the laboratory simulator (Figure 2) under cold and hot side temperatures of 50 °C and 500 °C, respectively.

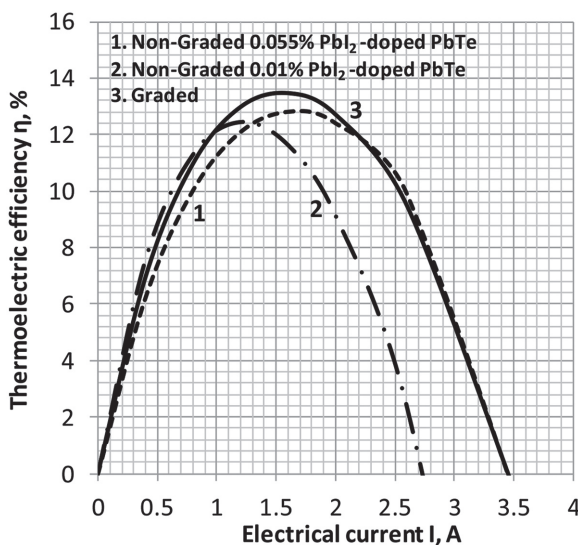


Figure 6. COMSOL simulated comparison between nongraded (curves 1 and 2) and graded (curve 3) thermoelectric module for 50/500 °C temperature range.

From this figure, it can be clearly seen that due to the increase in Carnot efficiency and the open-circuit voltage with increasing temperature difference, both the output electrical power and efficiency values increase up to ≈ 0.164 W couple $^{-1}$ and a remarkable value of $\approx 14\%$, respectively, for a hot side temperature of 500 °C. Such a high thermoelectric efficiency value for a couple operating between a cold side of 50 °C and a hot side of 500 °C is among the highest ever reported and even higher than the 11.5% value reported recently for similar non-FGM couples' compositions, following an analytical 1D simulation without taking into account the transport properties' temperature dependence and contact resistance contributions.^[1]

Figure 6 shows the calculated efficiencies of each of the non-graded samples (curves 1 and 2) in comparison to the graded composition (curve 3). This calculation emphasizes the great advantage of grading a thermoelectric material in order to achieve enhanced thermoelectric conversion efficiency.

5. Experimental Validation of the FEM

Based on the modeling results, an FGM thermoelectric, n-type leg was fabricated according to the scheme of Figure 1c. For validation of the obtained carrier concentration profile following hot pressing, and its agreement with the theoretical design without any adverse mutual diffusion effects, which might result in averaging of the carrier concentration along the entire leg, the Seebeck coefficient of this leg was scanned, as described in the experimental section, along the hot pressed graded samples. Figure 7 shows the Seebeck coefficient variation along the leg around room temperature, following hot pressing and additional thermal treatment at 500 °C for 100 h, simulating an extreme working condition, compared to the actual junction temperature of ≈ 200 °C between the two n-type segments.

This graph indicates that the designed concentrations profile was maintained following hot pressing (at 800 °C), with a

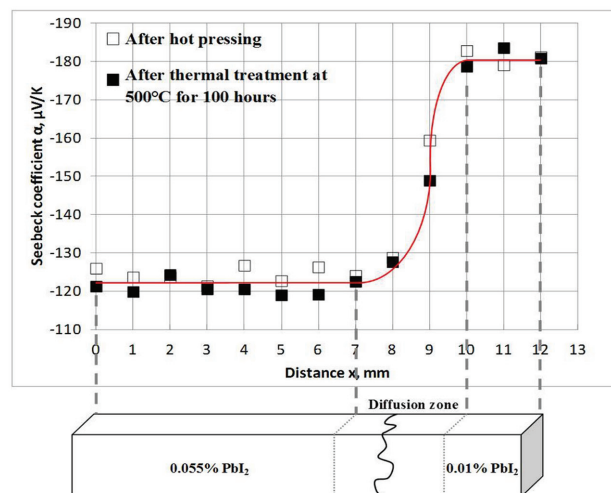


Figure 7. Variation of Seebeck coefficient values along n-type 0.01/0.055% PbI₂ doped (Pb_{0.95}Sn_{0.05}Te)_{0.92}(PbS)_{0.08} functionally graded materials, following hot pressing and 500 °C/100h thermal treatment.

reasonable (≈ 2 mm) interaction zone in proximity to the junction between the two segments. Nevertheless, no practical variations of the profile were observed following the maximal expected working condition (500 °C) for 100 h, highlighting the high stability and low diffusion rate of PbI₂ in PbTe-based materials, in agreement with previously reported data for pure PbTe compound at this temperature.^[27,28]

Applying a large (450 °C) temperature difference (hot side of 500 °C and cold side of 50 °C) on the investigated graded couple in the laboratory simulator, shown in Figure 2, resulted in the experimental points shown in Figure 5a. As can be seen by these results, a maximal electrical power of ≈ 0.145 W was experimentally observed, a $\approx 10\%$ lower value than that theoretically estimated (≈ 0.16 W), probably due to higher apparent contact resistances ($\approx 1.2 \times 10^{-3} \Omega \text{ mm}^2$) than the theoretically estimated in the model ($10^{-3} \Omega \text{ mm}^2$) thermal losses at the radial axis or measurement error at the material's transport properties measuring tools. Nevertheless, the good agreement between the experimentally and calculated electrical power values expected for the investigated graded thermoelectric couple can be clearly seen, highlighting its potential for being employed in practical energy conversion applications.

6. Conclusion

In the current manuscript, an n-type FGM based on a phase-separated (Pb_{0.95}Sn_{0.05}Te)_{0.92}(PbS)_{0.08} matrix doped with two PbI₂ concentrations of 0.01% and 0.055%, was developed by simultaneous hot pressing of the two compositions' powder. Up to ≈ 200 °C, the ZT values of the 0.01% doping concentration were higher compared to the 0.055% doping. However, beyond this temperature higher ZTs of up to 1.3 were obtained for the latter, providing the possibility for average ZT enhancement over a wide temperature range by grading both of the compositions. These high ZT values in each of the individual segments, compared to previously reported PbI₂-doped pure PbTe compounds, were

attributed to the generation of PbTe- and PbS-rich submicron phase separation features. For approaching a higher technology readiness level, beyond the materials development, toward the development of a direct thermal to electrical thermoelectric converter, a COMSOL finite-element thermoelectric simulation, taking into account temperature-dependent transport properties, contact resistances, and Thomson heat, was developed. Using an accurate and versatile thermoelectric model allows calculating the module performance under a variety of boundary conditions, geometries, and applications. The full analysis, taking into account all of the mentioned above contributions, indicates a remarkable thermoelectric efficiency of up to $\approx 14\%$ based on the developed n-type FGM legs and the previously reported phase separated p-type $\text{Ge}_{0.87}\text{Pb}_{0.13}\text{Te}$ composition, showing the highest ZT value ever reported to date. This impressive performance exhibits at least $\approx 20\%$ efficiency improvement compared to those previously reported for non-FGM couples based on similar compositions.

Acknowledgements

The work was supported by the Israel Science Foundation (ISF), Grant nos. 497/12 and 1578/12. The authors acknowledge Mr. Yair George for his great contribution to the synthesis of the alloys, homogeneous and graded samples preparation, and thermoelectric measurements.

Received: February 5, 2015
 Published online: April 10, 2015

- [1] Y. Gelbstein, J. Davidow, S. N. Girard, D. Y. Chung, M. Kanatzidis, *Adv. Energy Mater.* **2013**, *3*, 815.
- [2] Y. Gelbstein, Z. Dashevsky, M. P. Dariel, *Phys. Stat. Sol. (RRL)* **2007**, *1*, 232.
- [3] S. Gorsse, P. Bellanger, Y. Brechet, E. Sellier, A. Umarji, U. Ail, R. Decourt, *Acta Mater.* **2011**, *59*, 7425.
- [4] Y. Gelbstein, B. Dado, O. Ben-Yehuda, Y. Sadia, Z. Dashevsky, M. P. Dariel, *J. Electron. Mater.* **2010**, *39*, 2049.
- [5] Y. Gelbstein, G. Gotesman, Y. Lishzinker, Z. Dashevsky, M. P. Dariel, *Scr. Mater.* **2008**, *58*, 251.
- [6] Y. Gelbstein, Z. Dashevsky, M. P. Dariel, *J. Appl. Phys.* **2008**, *104*, 033702.
- [7] J. P. Heremans, V. Jovovic, E. S. Toberer, A. Saramat, K. Kurosaki, A. Charoenphakdee, S. Yamanaka, G. J. Snyder, *Science* **2008**, *321*, 554.
- [8] K. Biswas, J. He, Q. Zhang, G. Wang, C. Uher, V. P. Dravid, M. G. Kanatzidis, *Nat. Chem.* **2011**, *3*, 160.
- [9] K. Biswas, J. He, I. D. Blum, C.-I. Wu, T. P. Hogan, D. N. Seidman, V. P. Dravid, M. G. Kanatzidis, *Nature* **2012**, *489*, 414.
- [10] Y. Pei, X. Shi, A. LaLonde, H. Wang, L. Chen, G. J. Snyder, *Nature* **2011**, *473*, 66.
- [11] J. Androulakis, C.-H. Lin, H.-J. Kong, C. Uher, C.-I. Wu, T. Hogan, B. A. Cook, T. Caillat, K. M. Paraskevopoulos, M. G. Kanatzidis, *J. Am. Chem. Soc.* **2007**, *129*, 9780.
- [12] S. N. Girard, J. He, X. Zhou, D. Shoemaker, C. M. Jaworski, C. Uher, V. P. Dravid, J. P. Heremans, M. G. Kanatzidis, *J. Am. Chem. Soc.* **2011**, *133*, 16588.
- [13] H. Lin, E. S. Božin, S. J. L. Billinge, J. Androulakis, C. D. Malliakas, C. H. Lin, M. G. Kanatzidis, *Phys. Rev. B* **2009**, *80*, 045204.
- [14] J. He, S. N. Girard, M. G. Kanatzidis, V. P. Dravid, *Adv. Funct. Mater.* **2010**, *20*, 764.
- [15] Y. Gelbstein, *J. Appl. Phys.* **2009**, *105*, 023713.
- [16] Y. Gelbstein, B. Dado, O. Ben-Yehuda, Y. Sadia, Z. Dashevsky, M. P. Dariel, *Chem. Mater.* **2010**, *22*, 1054.
- [17] B. Dado, Y. Gelbstein, M. P. Dariel, *Scr. Mater.* **2009**, *62*, 89.
- [18] Y. Gelbstein, Y. Rosenberg, Y. Sadia, M. P. Dariel, *J. Phys. Chem. C* **2010**, *114*, 13126.
- [19] Y. Rosenberg, Y. Gelbstein, M. P. Dariel, *J. Alloys Compd.* **2012**, *526*, 31.
- [20] Y. Gelbstein, *J. Appl. Phys.* **2012**, *112*, 113721.
- [21] Y. Gelbstein, *Acta Mater.* **2013**, *61*, 1499.
- [22] T. M. Tritt, M. A. Subramanian, *MRS Bull.* **2006**, *31*, 188.
- [23] A. A. Volykhov, L. V. Yashina, V. I. Shtanov, *Inorg. Mater.* **2006**, *42*, 596.
- [24] A. Laugier, *Rev. Phys. Appl.* **1973**, *8*, 259.
- [25] J. S. Harris, J. T. Longo, E. R. Gertner, J. E. Clarke, *J. Cryst. Growth* **1975**, *28*, 334.
- [26] A. A. Volykhov, L. V. Yashina, M. E. Tamm, A. V. Ryzhenkov, *Inorg. Mater.* **2009**, *45*, 968.
- [27] Y. Gelbstein, Z. Dashevsky, M. P. Dariel, *Physica B* **2005**, *363*, 196.
- [28] Y. Gelbstein, Z. Dashevsky, M. P. Dariel, *Physica B* **2007**, *391*, 256.
- [29] D. Ebbling, M. Jaegle, M. Bartel, A. Jacquot, H. Böttner, *J. Electron. Mater.* **2009**, *38*, 1456.
- [30] H. Fahad, Md. Hasan, G. Li, Md. Hussain, *Appl. Nanosci.* **2013**, *3*, 175.
- [31] E. Sandoz-Rosado, R. Stevens, *J. Electron. Mater.* **2010**, *39*, 1848.
- [32] S. Zhou, B. G. Sammakia, B. White, P. Borgesen, *Int. J. Heat Mass Transfer* **2013**, *62*, 435.
- [33] A. Takezawa, M. Kitamura, *Int. J. Numer. Methods Eng.* **2012**, *90*, 1363.
- [34] H. J. Goldsmid, *Introduction to Thermoelectricity*, Springer Series in Materials Science, Heidelberg, Dordrecht, London, **2010**, p. 7E21.
- [35] A. Singh, S. Bhattacharya, C. Thinaharan, D. K. Aswal, S. K. Gupta, J. V. Yakhmi, K. Bhanumurthy, *J. Phys. D: Appl. Phys.* **2009**, *42*, 015502.